

A 3D Hermite-based multiscale local active contour method with elliptical shape constraints for segmentation of cardiac MR and CT volumes

Leiner Barba-J¹  · Boris Escalante-Ramírez¹ · Enrique Vallejo Venegas² · Fernando Arámbula Cosío³

Received: 4 January 2017 / Accepted: 4 October 2017 / Published online: 23 October 2017
© International Federation for Medical and Biological Engineering 2017

Abstract Analysis of cardiac images is a fundamental task to diagnose heart problems. Left ventricle (LV) is one of the most important heart structures used for cardiac evaluation. In this work, we propose a novel 3D hierarchical multiscale segmentation method based on a local active contour (AC) model and the Hermite transform (HT) for LV analysis in cardiac magnetic resonance (MR) and computed tomography (CT) volumes in short axis view. Features such as directional edges, texture, and intensities are analyzed using the multiscale HT space. A local AC model is configured using the HT coefficients and geometrical constraints. The endocardial and epicardial boundaries are used for evaluation. Segmentation of the endocardium is controlled using elliptical shape constraints. The final endocardial shape is used to define the geometrical constraints for segmentation of the epicardium. We follow the assumption that epicardial and endocardial shapes are similar in volumes with short axis view. An initialization scheme based on a fuzzy C-means algorithm and mathematical morphology was designed. The algorithm performance was evaluated using cardiac MR and CT volumes in short axis view demonstrating the feasibility of the proposed method.

Keywords Hermite transform · Directional and multiscale analysis · Active contour · Cardiac MR/CT volumes · Left ventricle segmentation

1 Introduction

Heart failures have become some of the major causes of death in developed and developing countries [11]. Detection of cardiac diseases during early stages of illness can be fundamental to preserve the life of patients. In this sense, cardiac imaging techniques such as MR and CT have become essentials for heart evaluation. Both technologies consist of noninvasive tests which provide a set of image slices of the heart. Several cardiac affections and conditions can be diagnosed with heart imaging techniques, including coronary artery diseases, affections provoked by heart attacks, heart muscle diseases, congenital defects, left ventricle (LV) dysfunction, heart valve diseases, ischemia, myocardial mechanical problems and others [4].

LV, within the cardiac structures, is of great concern for heart function evaluation [15, 32]. LV size at both end-diastolic (ED) and end-systolic (ES) phase is commonly used to identify cardiac failures [21]. Moreover, LV mass can be used as a predictor of morbidity and mortality in some patients [30]. Segmentation of the LV is required to quantify these variables. The need for automatic or semiautomatic algorithms is justified by the fact that manual delineation is tedious, time consuming and observer-dependent. More objective measurements can be achieved by using robust computer-aided segmentation methods.

LV segmentation using cardiac images is a problem that researchers have tried to solve for many years. Although many algorithms have been proposed, this problem still remains as an open issue [32].

✉ Leiner Barba-J
lebaji@gmail.com

¹ Facultad de Ingeniería, Universidad Nacional Autónoma de México, C.U., México, D.F., Mexico

² Hospital Ángeles del Pedregal, Cardiología, México, D.F., Mexico

³ Centro de Ciencias Aplicadas y Desarrollo Tecnológico, CCADET, Universidad Nacional Autónoma de México, C.U., México, D.F., Mexico

Active contours (ACs) are some of the most accepted methods for medical image segmentation. They consist of evolving interfaces guided by internal and external forces which depend on geometrical and image features [14]. In these methods, the segmentation process is generally modeled as energy functionals whose terms are designed to stop the interface evolution at the object boundaries.

External forces in ACs need for efficient methods to extract image features which are used to guide the evolution of the interfaces. Although many methods have been proposed for this purpose (boundary-based techniques [9], region-based approaches [10], methods based on probabilistic interpretation [31] and others), all of them attempt to analyze image features using the original space. Multiscale and multiresolution analysis have demonstrated being very powerful strategies to extract features in medical image applications [1]. In this work, we use the 3D Hermite transform for data characterization. It consists of a powerful mathematical tool that projects a function onto the space composed by the Hermite polynomials [28]. Local and directional analysis [18], as well as multiscale and multiresolution analysis [43] can be competently performed with the HT.

In this work, a novel 3D AC model embedded into the HT space is proposed. Features such as intensities, boundary information, and geometrical constraints are combined using a hierarchical multiscale scheme. Intensity and boundary information are directly computed from coefficients of the HT while shape-based constraints are based on the AC properties. We exploit some advantages of the HT to provide local directional and multiscale analysis. We use elliptical shapes for geometrical constraint. An initialization stage using a fuzzy C-means algorithm, combined with morphological operations, is also employed. The proposed method is experimentally evaluated using MR and CT studies. We demonstrate that combining different energy models into a multiscale strategy based on the HT, cardiac volumes can be efficiently processed.

1.1 Related works

There have been numerous contributions about segmentation methods applied to LV in cardiac MR/CT images [15, 32, 47]. Implicit [5, 22, 26, 33, 34, 49, 52] and parametric [24, 37, 44, 50] ACs, probabilistic algorithms [13, 42], statistical shape models [2, 3, 8, 20], and atlas-based algorithms [6, 7] are the most typical methods used for LV segmentation.

Statistical shape models such as ASMs (active shape models) and AAMs (active appearance models) use a set of sample shapes to train a statistical model which is subsequently used for segmenting new data. Hans van Assen et al. [3] combined a 3D ASM with a C-means algorithm to

segment the LV in MR volumes. Data with lack of information can be segmented with this method. Ecabert et al. [17] developed an approach to extract four cavities of the heart as well as the myocardium and great vessels using CT volumes. The method uses an ASM-based parametric model with prior information. Although these methods are efficient for segmentation of cardiac data, their performances depend on the number of training samples.

Parametric ACs have been mainly employed for segmentation of cardiac images. They consist of parametric curves which move with a velocity field depending on image features and geometrical information. Wu et al. [50] used a classical snake model for LV segmentation in MR images. Here, edges are detected using an external force called gradient vector convolution. Circular shape constraints are used. The problem with methods based entirely on edge detectors is the sensitivity to noise. Sliman et al. [44] proposed a method for 2D segmentation of the myocardium using a parametric AC which combines two terms: a first-order combination of discrete Gaussians and a second-order Markov-Gibbs random field. A distance measure was also incorporated to maintain a minimal separation between both contours.

ACs based on level sets acquired much relevance for segmentation of medical images. Unlike parametric ACs, curves and interfaces are represented implicitly using level sets. Easy implementation, extension to higher dimensions, and possibility to combine different types of energies in a transparent way are the most typical advantages of level set methods. Changes of configuration are also assumed naturally. In [22], the LV endocardium was segmented using a Local Binary Fitting (LBF) energy functional [27] and a convex hull algorithm while a dynamic programming method was used for the epicardium. However, the method does not use shape energies. A variational method is presented in [5] in which two curves are evolved to extract the endocardium and epicardium. A prior term is used to model the overlapping intensities in all regions of the LV. Shape-based energies are not used which may hinder the segmentation of papillary muscles. In contrast, Pluempitiwiriyaew et al. [34] proposed a level set functional which includes a region term, a boundary term, a regularization term and a shape term. In the latter, they assume the LV can be modeled using an elliptical shape. However, inhomogeneity problems of cardiac images are not considered. Attempting to model similarity between the LV cavity and epicardial boundary, Woo et al. [49] designed a multiphase level set approach to segment the endocardium and epicardium. The method includes a shape prior based on the discrepancy between both regions, which is assumed to follow a Gaussian distribution. Zhu et al. [51] presented a combination of thresholding, mathematical morphology, geometrical operations and classical AC methods [9] to

segment the endocardium and epicardium in 3D cardiac CT studies. The poor contrast between the myocardium and surrounding tissues in cardiac CT studies affects the performance of classical AC models.

Other researches have recently opted for dynamic programming models [23, 35, 41], registration-based methods [48], random walk [19], and sparse modeling [36]. In spite of all the described methods attempt to settle the segmentation problem of the LV, they use image features obtained from the original space of the input data. Nonetheless, most of them do not use shape prior, they need of a huge dataset to train a model and image inhomogeneities are not considered. Even more, segmentation of cardiac images has been mainly focused on analyzing either MR or CT images without generalization to both types of modalities.

1.2 Challenges in LV segmentation

Although many works have been proposed, the segmentation of the LV remains as an active field of research. Different types of problems are found when segmenting the LV in cardiac MR/CT data. Variations of contrast, irregular shapes of the endocardial and epicardial boundaries, diffuse edges, inhomogeneities, lack of information at apex and base of the heart and noise are the most common difficulties to be handled by segmentation algorithms in these types of images [47]. There is also a main consensus about the assumption that papillary muscles are considered part of the LV cavity for measurement purposes, which additionally imposes a great challenge for segmentation approaches [15].

Other common trouble we can find is this type of application is the difficulty to address extensive and objective comparisons among many algorithms. Some collaborative works and workshops have significantly contributed to the field of LV segmentation using MR studies because they have provided public datasets and evaluation protocols for use of the researcher community. The MICCAI 2009

challenge [46], designed to perform valuable competitions of LV segmentation algorithms, is perhaps the most known workshop organized for this purpose. Nonetheless, a more recent initiative called the cardiac atlas project [45] was created to provide a huge database of annotated cases with the objective that researchers prove their algorithms. These collaborative works are also useful because they allow the researchers to evaluate the performance of several methodologies for this specific application. Despite the effort made, the LV segmentation using MR data remains as an open issue. In many cases, authors have decided to use their own set of data, and they also used different metrics for evaluation. Regarding cardiac CT studies, there are not public datasets which imposes a bigger challenge for evaluating segmentation algorithms.

2 Method

The developed method consists of a 3D local AC model embedded into a hierarchical multiscale scheme provided by the HT applied to LV segmentation in cardiac MR/CT volumes. Coefficients of the HT guide the AC evolution. The LV cavity is modeled using elliptical functions which are incorporated into the shape energy. An endocardial-based shape energy is employed for segmentation of the epicardium based on the assumption that epicardial and endocardial shapes are similar. The process follows a coarse-to-fine segmentation. The endocardium is segmented first followed by the epicardium. An initialization method is proposed using a fuzzy C-means algorithm combined with mathematical morphology operations. The general diagram of the designed method is depicted in Fig. 1. The 3D HT is calculated for the input volume using several scales. Coefficients are posteriorly steered. The initialization algorithm is then runned in order to obtain the initial surface at the largest scale. Here, the AC model is used iteratively. Once

Fig. 1 Scheme of the proposed segmentation method

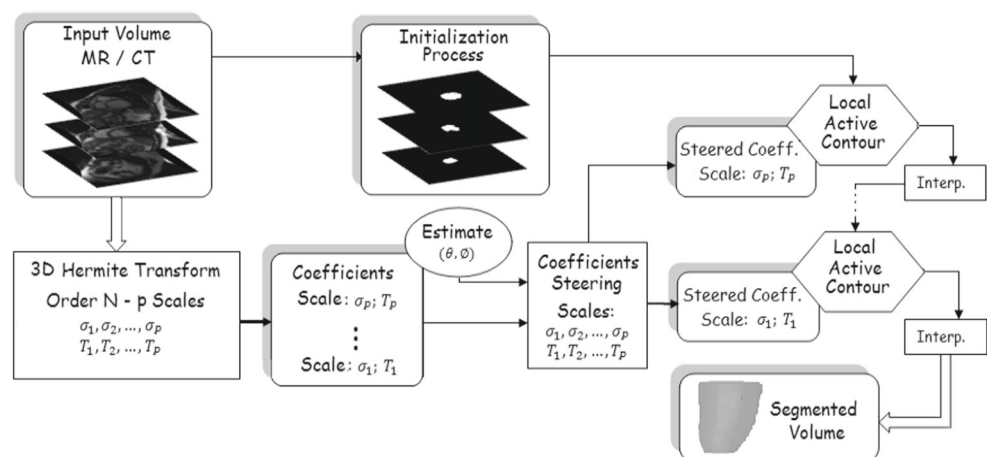


Table 1 List of coefficients, 3D HT until order $n = 2$

Order n	m	l	Coefficient
$n = 0$	$m = 0$	$l = 0$	$L_{0,0,0}$
$n = 1$	$m = 0$	$l = 0$	$L_{1,0,0}$
		$l = 1$	$L_{0,0,1}$
		$l = 2$	$L_{0,0,2}$
$n = 2$	$m = 0$	$l = 0$	$L_{2,0,0}$
		$l = 1$	$L_{1,0,1}$
	$m = 1$	$l = 0$	$L_{0,1,0}$
		$l = 1$	$L_{0,1,1}$
	$m = 2$	$l = 0$	$L_{0,2,0}$
		$l = 1$	$L_{0,2,1}$

the AC has converged, its result is interpolated and used as initialization for the next scale. These steps are repeated until reaching the finest scale. Each stage of the proposed framework will be described in this section.

2.1 The 3D Hermite transform (HT)

The goal of the 3D HT is to project the input volume onto the space of Hermite polynomials in order to extract relevant information [28]. Let $f(x, y, z)$ be a 3D input function, its 3D HT is computed as follows:

$$L_{n-m,m-l,l}(p, q, r) = \int_{-\infty}^{\infty} f(x, y, z) V^2(x-p, y-q, z-r) \cdot G_{n-m,m-l,l}(x-p, y-q, z-r) dx dy dz \quad (1)$$

where $L_{n-m,m-l,l}(p, q, r)$ are the 3D cartesian Hermite coefficients, $V(x, y, z)$ is an isotropic 3D Gaussian window with standard deviation σ and $G_{n-m,m-l,l} = W H_{n-m}(\frac{x}{\sigma}) H_{m-l}(\frac{y}{\sigma}) H_l(\frac{z}{\sigma})$ correspond to the normalized

3D Hermite polynomials which are orthogonal with respect to $V^2(x, y, z)$, and $W = \frac{1}{\sqrt{2^{n-m} (n-m)! (m-l)! l!}}$. Coefficients are calculated for subscripts $n = 0, 1, \dots, N$; $m = 0, 1, \dots, n$ and $l = 0, 1, \dots, m$ where n is the order of the transform. Implementation of the 3D HT can be performed by convolving the input function with the set of Hermite filters defined as:

$$D_{n-m,m-l,l}(x, y, z) = V^2(x, y, z) G_{n-m,m-l,l}(x, y, z) = W \frac{d^{n-m}}{d(\frac{x}{\sigma})^{n-m}} \frac{d^{m-l}}{d(\frac{y}{\sigma})^{m-l}} \frac{d^l}{d(\frac{z}{\sigma})^l} V^2(x, y, z) \quad (2)$$

and subsequently subsampling at positions (p, q, r) . For simplicity, we will use $T = p = q = r$ as the subsampling variable. The list of coefficients obtained for the 3D HT until order $n = 2$ are depicted in Table 1.

The subsampling T and the standard deviation σ are the free parameters to be configured. The latter determines the scale of the transformation. In this work, we use a hierarchical multiscale framework in which the 3D HT is computed using several values of σ and T . Here, a specific value of T is used for each value of σ . Then, the multiscale scheme is defined by the couple (σ_j, T_j) , with $j = 1, 2, \dots, p$ where p is the maximum number of scales. The first coefficient $L_{0,0,0}$ consists of a smoothed version of the input volume while coefficients corresponding to order $n = 1$ are edge maps. Coefficients of higher order, $n > 1$, are very suitable to analyze texture of the input data. Figure 2a illustrates an example of the 3D HT until order $n = 1$ applied to a cardiac MR volume using two scales ($\sigma_1 = 1, T_1 = 1$; $\sigma_2 = 1.5, T_2 = 2$). Slices show the middle of the LV.

In general, one of the main advantages of the HT is its ability to perform local directional analysis [18, 43]. Cartesian coefficients of order $n \geq 1$ obtained using Eq. 1 can

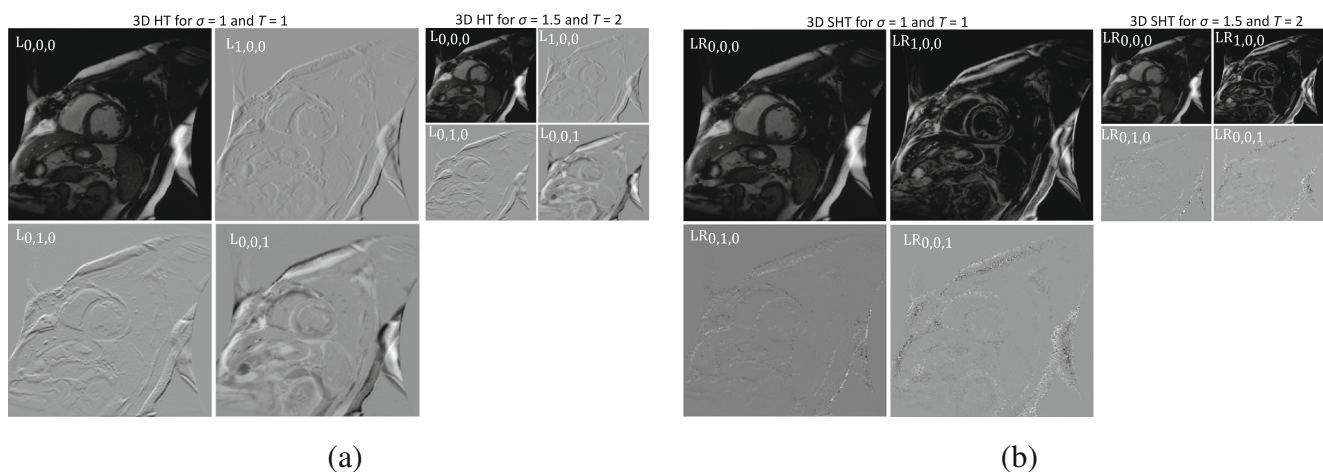


Fig. 2 Coefficients of the 3D HT applied to a cardiac MR volume. Slices show the middle of the heart. **a** Cartesian coefficients. **b** Steered coefficients

be steered using a linear combination of them. Patterns such as edges and textures of the input data are better described by performing directional analysis. Two angles, θ and ϕ , are needed in order to perform the steering process. The first angle defines the rotation w.r.t. $xy - plane$ and the second angle w.r.t. $z - axis$. Therefore, coefficients are steered as follows:

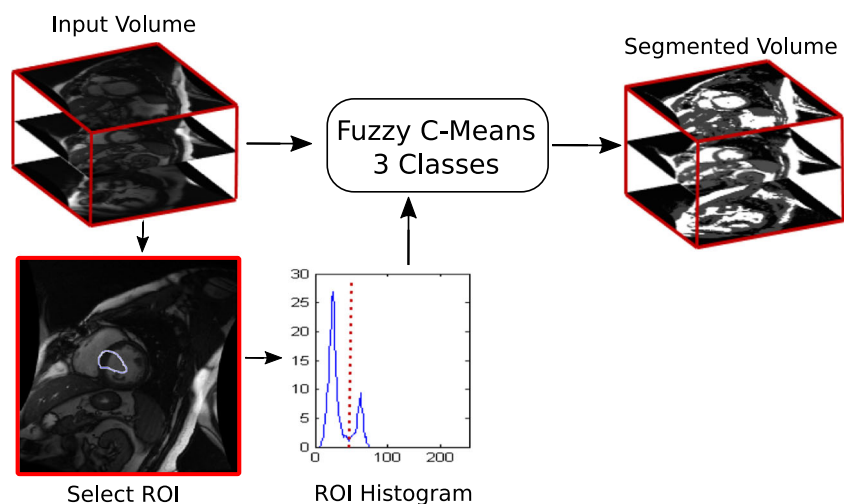
$$LR_{n-m,m-l,l}(\theta, \phi) = \sum_{k=0}^n \sum_{s=0}^k C_{m,l,k,s}^{(n)}(\theta, \phi) L_{n-k,k-s,s} \quad (3)$$

where $C_{m,l,k,s}^{(n)}(\theta, \phi)$ represents a set of coefficient values used for the steering process, $L_{n-k,k-s,s}$ are the cartesian Hermite coefficients and $LR_{n-m,m-l,l}(\theta, \phi)$ are the steered Hermite coefficients. Figure 2b illustrates the steered Hermite coefficients obtained from the cartesian coefficients shown in Fig. 2a. It can be seen that most of the energy is concentrated in coefficient $LR_{1,0,0}$. It is a frequent practice to use only the steered coefficients $LR_{1,0,0}(\theta, \phi)$, $LR_{2,0,0}(\theta, \phi)$, \dots , $LR_{n,0,0}(\theta, \phi)$ meanwhile the rest of them are discarded, which means that a denoising process is indirectly being applied.

2.2 Proposed initialization

The initial shape must be carefully selected when using local AC models [25]. For this purpose, we have designed a novel semi-automatic initialization scheme which combines a fuzzy C-means method [12] with morphological operators. Figure 3 graphically outlines this scheme. Firstly, we manually define limits for base and apex of the LV. The histogram of the image corresponding to middle of the LV is processed to obtain initial average values for the LV cavity and myocardium. A fuzzy C-means algorithm is then applied to segment the volume in three classes: (1) background, (2) myocardium and similar tissues, and (3) LV cavity and similar tissues. Figure 3 briefly describes the initial process.

Fig. 3 First stage of the initialization based on a fuzzy C-means algorithm



Once the input volume is processed using the fuzzy C-means algorithm, we need to compute the initial surfaces for the endocardium and epicardium. This process is performed using two separate algorithms.

Endocardium initialization The schematic diagram of this algorithm is illustrated in Fig. 4a. For each slice of the pre-segmented volume with fuzzy C-means, we proceed as follows:

- Each object corresponding to third class is labeled.
- Circularity Cr , area A and center of mass Cm measurements are used to determine the object corresponding to the LV cavity which is selected according to three conditions: $Cr > Tc$, $A > Ta$ and Cm being the most central object satisfying the other two conditions. Tc and Ta are two thresholds.
- When all volume slices have been processed, the initial endocardial surface is constructed.

Epicardium initialization Segmentation results of the endocardium are also incorporated as input information to initialize the epicardium. Figure 4b describes the general scheme. Similarly, for each slice of the volume resulted from the fuzzy C-means stage, we proceed as follows:

- Take the second class as the region of interest. The rest of the image is assumed to be background.
- Small objects (smaller than the LV cavity) of the background are removed. This operation helps to remove, from the myocardial region, small artifacts resulted from the fuzzy C-means stage.
- An edge detector algorithm is used. The objective is to detect edge points of the epicardium.
- Using the center of mass of the LV cavity previously segmented, we divide the complete slice in four regions.

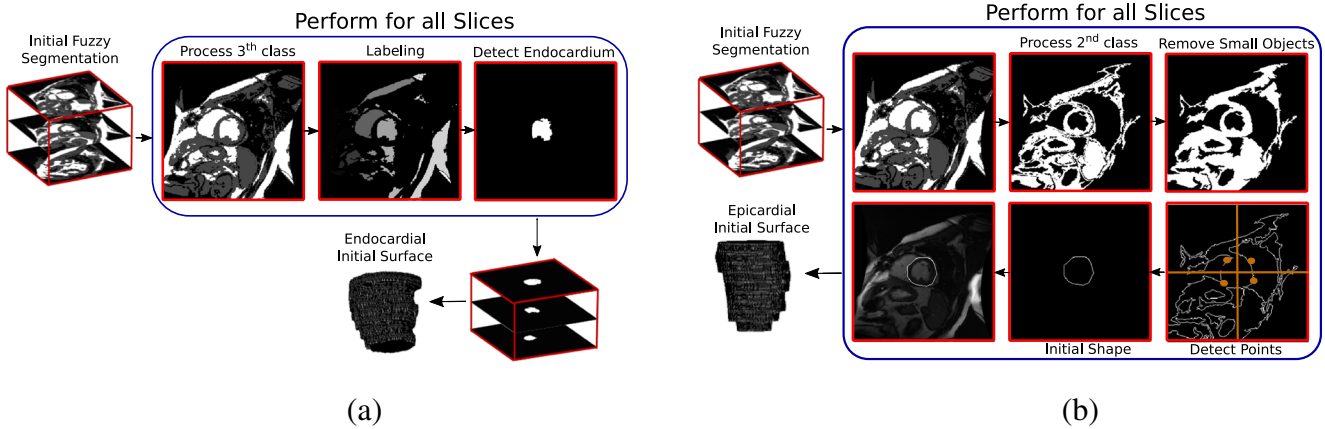


Fig. 4 **a** Endocardial initialization scheme, **b** Epicardial initialization scheme

- The contour points closest to the center of mass for each region are selected. Then, the initial shape is built at a distance d from the endocardial boundary using as reference the four contour points.
- Finally, the initial surface of the epicardium is built when all slices have been processed.

2.3 Proposed active contour model

We have designed an AC model with five energy functions: two region terms (one local and one global), an edge-based term and two geometrical terms. The first three energies incorporate coefficients of the HT which guides the AC evolution. The designed energy functional is used to segment the endocardial and epicardial boundaries. The AC has been represented using level sets [29]. Let $C = C(X)$, $X \in R^3$ be a moving interface which fragments the volume space Ω into two regions. It can be represented as the zero level set of a higher dimensional function, $C = \{X|\varphi(X) = 0\}$. The following convention has been adopted for the level set function: $\varphi(X) > 0$ for X outside C , $\varphi(X) < 0$ for X inside C , and $\varphi(X) = 0$ for $X \in C$. The general proposed energy functional is written as follows:

$$E = \lambda_1 E_L + \lambda_2 E_G + \lambda_3 E_B + \lambda_4 E_S + \lambda_5 E_R \tag{4}$$

where E_L and E_G are the local and global energy functions, E_B is the boundary-based energy, E_S is the shape constraint and E_R is the regularization term. Weight parameters $\lambda_m, m = 1, \dots, 5$ control the contribution of each energy term. All energy terms will be described in this section.

2.3.1 Local region energy

In general, inhomogeneities are frequent issues found in MR/CT images. Classical region-based AC models [10, 31] fail to segment objects with intensity inhomogeneities

because they are based on global features. Several previous works based on local level sets have attempted to solve the problem of image inhomogeneity [25, 27]. In this work, we used a local energy term E_L to characterize each point p of the input volume using information of its neighborhood. Taking a squared window W centered on each voxel, two regions are selected: inside (Ω_{in}) and outside (Ω_{out}) the current interface. We then compute the averages μ_1 and μ_2 for both regions respectively. Figure 5 outlines this modeling process. For visualization purposes the scheme is presented in 2D, however it is similar in 3D. The Hermite coefficient of order $n = 0$ is used as input volume.

The energy term is defined as:

$$E_L(\mu_1, \mu_2, \varphi) = \int_{\Omega} (L_{0,0,0}(X) - \mu_1(X))^2 H(\varphi(X)) dX + \int_{\Omega} (L_{0,0,0}(X) - \mu_2(X))^2 (1 - H(\varphi(X))) dX \tag{5}$$

where μ_1 and μ_2 are calculated as follows:

$$\mu_1(X) = \frac{\int_W I(X) H(\varphi(X)) dX}{\int_W H(\varphi(X)) dX}$$

$$\mu_2(X) = \frac{\int_W I(X) (1 - H(\varphi(X))) dX}{\int_W (1 - H(\varphi(X))) dX}$$

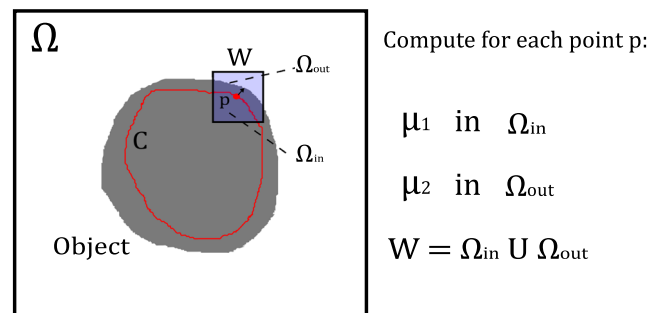


Fig. 5 Data modeling in the local region energy

where $I(X) = \{L_{0,0,0}(X)|X \in W\}$. The level set is regularized using Heaviside $H_\epsilon(z) = \frac{1}{2} \left(1 + \frac{2}{\pi} \tan^{-1} \left(\frac{z}{\epsilon}\right)\right)$ and Delta Dirac $\delta(z) = \frac{d}{dz}(H(z))$ functions for minimization purposes [10]. The terms $H(\varphi(X))$ represents the region inside the interface, and $(1 - H(\varphi(X)))$ is the outer region. Because the zero-order Hermite coefficient is used as input data, a noise reduction process is indirectly introduced in this energy term.

2.3.2 Global region energy

A global energy term is incorporated to strengthen the AC evolution, particularly in homogeneous regions. We adopted the classical energy functional based on probabilistic models [14, 31]. Assuming the input volume V is the result of a stochastic process, the partition $P(\Omega)$ of V can be obtained by optimizing the a posteriori probability $p(P(\Omega)/V)$ [31]. Considering the binary case of two independent regions, Ω_1 and Ω_2 (object and background), the global region energy is defined as follows:

$$E_G(\varphi) = - \int_{\Omega} \log(p(L_{0,0,0}(X)/\Omega_1))H(\varphi(X))dX + \int_{\Omega} \log(p(L_{0,0,0}(X)/\Omega_2))(1-H(\varphi(X)))dX \tag{6}$$

where $p(L_{0,0,0}(X)/\Omega_i)$ with $i = 1, 2$ is the probability function assumed for each partition. Similarly, the zero-order Hermite coefficient is used as input volume.

2.3.3 Boundary-based energy

The boundary-based energy aims at stopping the moving interface when edges are reached. Due to its simplicity and efficiency, we used the following functional:

$$E_B(\varphi) = \int_{\Omega} gH(\varphi(X))dX \tag{7}$$

where $g = \frac{1}{(1+LR_{1,0,0})}$. The steered coefficient $LR_{1,0,0}$ is used as input data in this energy term. Since it consists of a

local directional boundary detector, the edge map of the analyzed volume is captured efficiently for all orientations. This energy term takes advantage of the directional properties of the HT.

2.3.4 Shape constraint

Generally speaking, it is a common practice to employ geometrical shapes to model structures in medical images. LV segmentation in cardiac volumes becomes challenging due to presence of the papillary muscles which are considered to be part of the LV cavity. Moreover, subtle edges, low contrast as well as lack of information in some regions of the endocardium and epicardium impose more challenges for segmentation algorithms. Some authors have adopted elliptical [34] or circular [50] shapes to model the LV in cardiac MR/CT data with short axis view. In this work, we also consider that the LV cavity can be represented using elliptical shapes in all volume slices from base to apex. Our goal is to maintain a regular shape of the interface by controlling its deformation. This process is performed for each slice. The current 3D zero level set is then mapped to 2D zero level sets, see Fig. 6. Afterwards, an ellipse for each plane is estimated using each contour slice. Finally, we build a stack of signed distance functions from contours of the estimated ellipses.

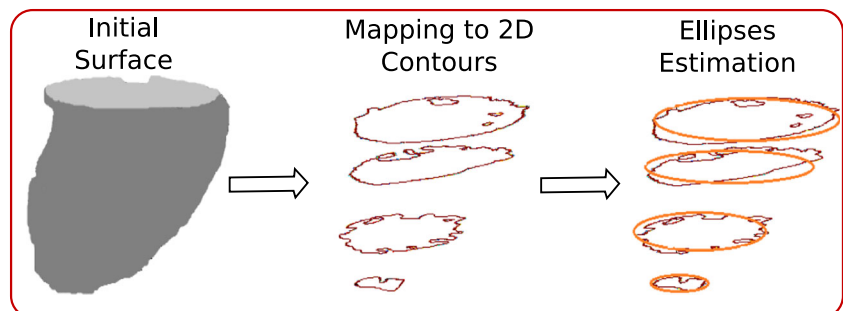
The ellipses estimation process is performed using the simple but effective method described in [39]. The stack of ellipses-based signed distance functions φ_s is compared with the original level set which allows penalizing the AC deformation when it differs from the elliptical shapes. For this purpose, we used the following energy functional [40]:

$$E_S(\varphi_s, \varphi) = \int_{\Omega} (\varphi(X) - \varphi_s(X))^2 H(\varphi(X))dX \tag{8}$$

The shape constraint consists of a geometrical function that only depends on the interface.

For the epicardial boundary, we assume that shape of the epicardium is similar to shape of the endocardium. The final segmentation of the endocardial boundary is then coded as φ_s . Therefore, when segmenting the epicardial boundary

Fig. 6 Ellipses estimation process. The initial surface is mapped to 2D contours and ellipses are estimated for each xy -plane



this energy term penalizes the deviation of the AC from the endocardial shape.

2.3.5 Regularization energy

We also include a regularization term which is normally used to privilege smooth interfaces in the segmentation process [9, 10, 14, 29, 31]. It is defined as:

$$E_R(\varphi) = \int_{\Omega} |\nabla H(\varphi(X))| dX \quad (9)$$

where ∇ is the gradient operator.

2.3.6 Energy minimization

The complete energy functional is a weighted combination of the described energy terms, see Eq. 4. It is well known that minimizing the complete functional is equivalent to minimizing each energy term separately and then performing the corresponding combination [49]. Fixing μ_1 , μ_2 and φ_s , using the calculus of variation and the steepest descent

method, the differential equation which minimizes E with respect to φ is obtained:

$$\begin{aligned} \frac{\partial \varphi}{\partial t} = & \left[\lambda_1 \left(- (L_{0,0,0} - \mu_1)^2 + (L_{0,0,0} - \mu_2)^2 \right) \right. \\ & + \lambda_2 \left(\frac{\log(p(L_{0,0,0}/\Omega_1))}{\log(p(L_{0,0,0}/\Omega_2))} \right) + \lambda_3 g \\ & \left. + \lambda_4 \text{Div} \left(\frac{\nabla \varphi}{|\nabla \varphi|} \right) \right] \delta(\varphi) - 2\lambda_5 H(\varphi)(\varphi - \varphi_s) \quad (10) \end{aligned}$$

2.4 Implementation details

Regarding the 3D HT, coefficients were steered using a criterion of maximum energy. Two or three scales were used depending on the input data.

For the level set implementation, we used a narrow band algorithm since the final segmentation is only defined by the zero level set. In the global term E_G , we assume Gaussian distributions whose parameters were computed from results of the initialization algorithm. All energy terms have been

Fig. 7 Image examples used for validation. Images show the LV at base (left), middle (center) and apex of the heart (right)

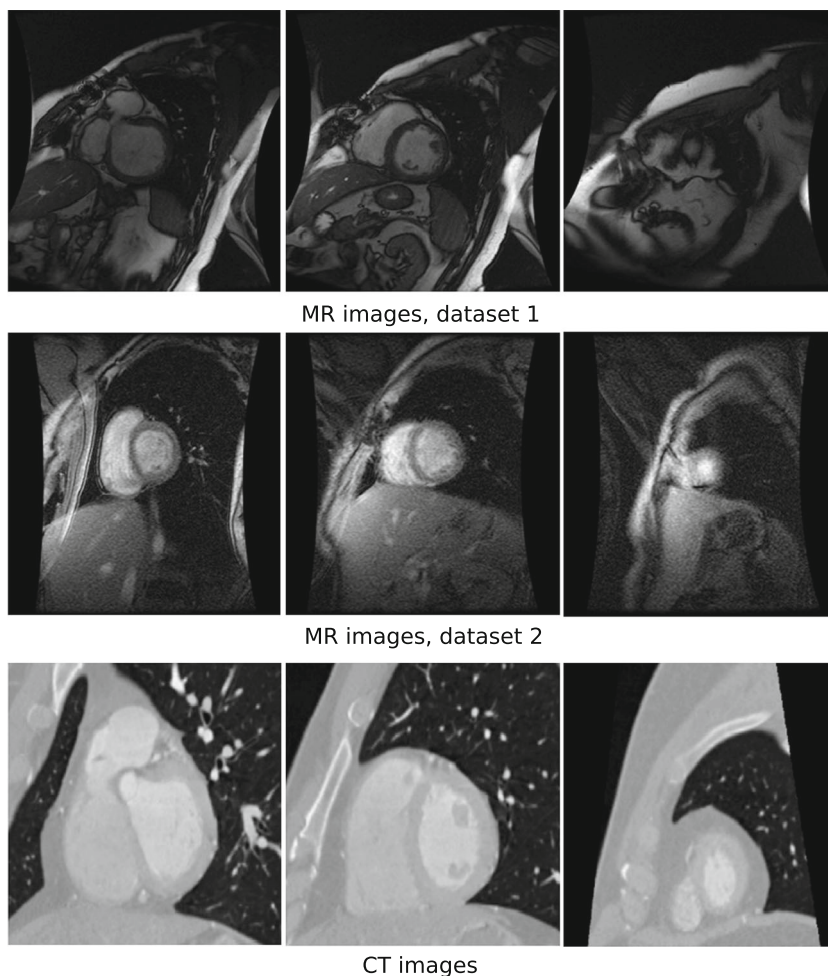


Table 2 Parameters configuration of the proposed algorithm

Parameters	Values	Description
MR Datasets		
$\sigma_j, j = 1, 2$	$\sigma_1 = 1.0; \sigma_2 = 1.5$	Two scales
$T_j, j = 1, 2$	$T_1 = 1; T_2 = 2$	
λ_m	$\lambda_1 \quad \lambda_2 \quad \lambda_3 \quad \lambda_4 \quad \lambda_5$	
$m = 1, 2, \dots, 5$	Endo 0.4–0.7 0.1–0.3 0.1–0.3 0.01 0.001–0.005	Range of weight values
$V_p(x, y, z)$	Epi 0.0 0.2–0.5 0.3–0.5 0.2 0.100–0.300	Window size
	Endo [7 7 1], [3 3 1]	
	Epi [10 10 0]	
CT Dataset		
$\sigma_j, j = 1, 2, 3$	$\sigma_1 = 1.2; \sigma_2 = 1.8; \sigma_3 = 2.4$	Three scales
$T_j, j = 1, 2, 3$	$T_1 = 1; T_2 = 2; T_3 = 4$	
λ_m	$\lambda_1 \quad \lambda_2 \quad \lambda_3 \quad \lambda_4 \quad \lambda_5$	
$m = 1, 2, \dots, 5$	Endo 0.2–0.5 0.5–0.8 0.0–0.1 0.01 0.01–0.05	Range of weight values
$V_p(x, y, z)$	Endo [15 15 1], [4 4 1], [3 3 1]	Window size

normalized within the range [0, 1]. In order to stop the AC evolution, we used the following criterion:

$$\left| \int_{\Omega} H(\varphi_{k_1}(X)) dX - \int_{\Omega} H(\varphi_{k_2}(X)) dX \right| < \tau \quad (11)$$

where k_1 and k_2 represent two different iterations with $k_2 = k_1 + q, q \in \mathbb{Z}^+$ and τ is a threshold.

The shape energy maintains a regular deformation of the AC during evolution. Since it does not depend on image features, it cannot guide the contour toward the boundaries of the object. For this energy term, we have used a double configuration: a small weight value is assigned to this energy at the beginning of the evolution and for a specific number of iterations. This weight is subsequently incremented. With this configuration, the AC is freely deformed during the first iterations and then adjusted to maintain the geometrical shape defined for the processed object.

3 Results

In this section, we present the results obtained with the proposed algorithm using MR/CT studies. Comparisons with other methods are also presented. Several metrics were used for evaluation: point-to-curve distance (PCD), point-to-surface distance (PSD), modified Hausdorff distance (MHD) [16] and the Dice similarity coefficient (DSC). Moreover, clinical indices were also used for evaluating the algorithm.

3.1 Materials

Two sets of MR and one of CT cardiac volumes were used for validation. The first set of MR data consists of 15

patients selected from the MICCAI challenge database [46]. These images were acquired with a 1.5T GE Signa MRI during 0–15 second breath-holds with 20 cardiac phases as temporal resolution over the complete cardiac cycle. Images were acquired in short axis view. The number of slices for each volume varies between 6 and 12 from the atrioventricular ring to the apex (thickness = 8 mm, gap = 8 mm, FOV = 320 mm 320 mm, matrix = 256 × 256).

The second set of MR data is composed by 15 patients selected from the database shared by [2]. Similarly, images were acquired with a GE Genesis Signa MR scanner. For each patient, 20 volumes describe the entire cardiac cycle. The number of slices ranges between 8 and 15. Each image slice consists of 256 × 256 pixels with pixel-spacing values between 0.93 and 1.64 mm. Spacing-between slices ranges from 6 to 13 mm.

We also used a cardiac CT dataset consisting of 15 patients. Tomographic studies were acquired with a SIEMENS 16-slice CT system. The scanner is composed of 128 detectors and synchronized with the ECG signal. Each image consists of 512 × 512 pixels, quantized to 12 bits × pixel. There are 10 volumes for each patient describing the entire cardiac cycle from diastole to systole.

Table 3 DSC obtained using segmentation results of four methods, including the proposed approach. Evaluation made using images of MR dataset 1

	Endocardium	Epicardium
Method 1 [23]	0.890 ± 0.030	0.940 ± 0.020
Method 2 [41]	0.869 ± 0.042	0.921 ± 0.020
Method 3 [35]	0.886 ± 0.039	0.928 ± 0.016
Our Method	0.910 ± 0.018	0.939 ± 0.009

Table 4 Average PCD, MHD and PSD (mm) obtained for the endocardial and epicardial segmentation using MR data

	PCD	MHD	PSD
MR Dataset 1			
Endocardium	1.5430 ± 0.4371	3.2342 ± 1.7985	0.8859 ± 0.2747
Epicardium	1.6204 ± 0.3374	3.3062 ± 1.3570	0.8472 ± 0.1557
MR Dataset 2			
Endocardium	1.2731 ± 0.2652	2.0147 ± 1.1707	0.6172 ± 0.1295
Epicardium	1.6287 ± 0.2545	3.1348 ± 1.0244	0.8005 ± 0.1586

Figure 7 shows image examples taken from each dataset. It can be noted the high variability regarding the image features.

3.2 Parameters selection

In this work, we used experimental tests in order to determine the best set of parameters to configure the algorithm. Free parameters in the Hermite-based multiscale stage are the scales and subsampling values controlled by σ and T . In the level set functional, we must assign weight values

for each energy term. In our experiments, parameters of the HT were fixed while parameters of the AC functional were configured for each test. Table 2 describes the algorithm configuration. Values were assigned depending on the dataset.

3.3 MR volumes

Results using the first set of MR data using the DSC metric are presented in Table 3. The DSC was computed for all slices at ED and ES phase for each patient. Results are finally averaged for all patients and presented separately for the endocardium and epicardium. The best result for the endocardium was 0.9387 and the worst 0.8323. Similarly, for the epicardium we obtained a maximum DSC of 0.9441 and a minimum of 0.8824. Comparisons with other methods which have used the same dataset are presented in Table 3 as well. It can be noted that our method achieved better results as those reported in the state of art.

Results obtained for the first and second dataset using the PCD and MHD metrics are presented in Table 4. A Box-Plot graph (see Fig. 8) shows the behavior of the proposed

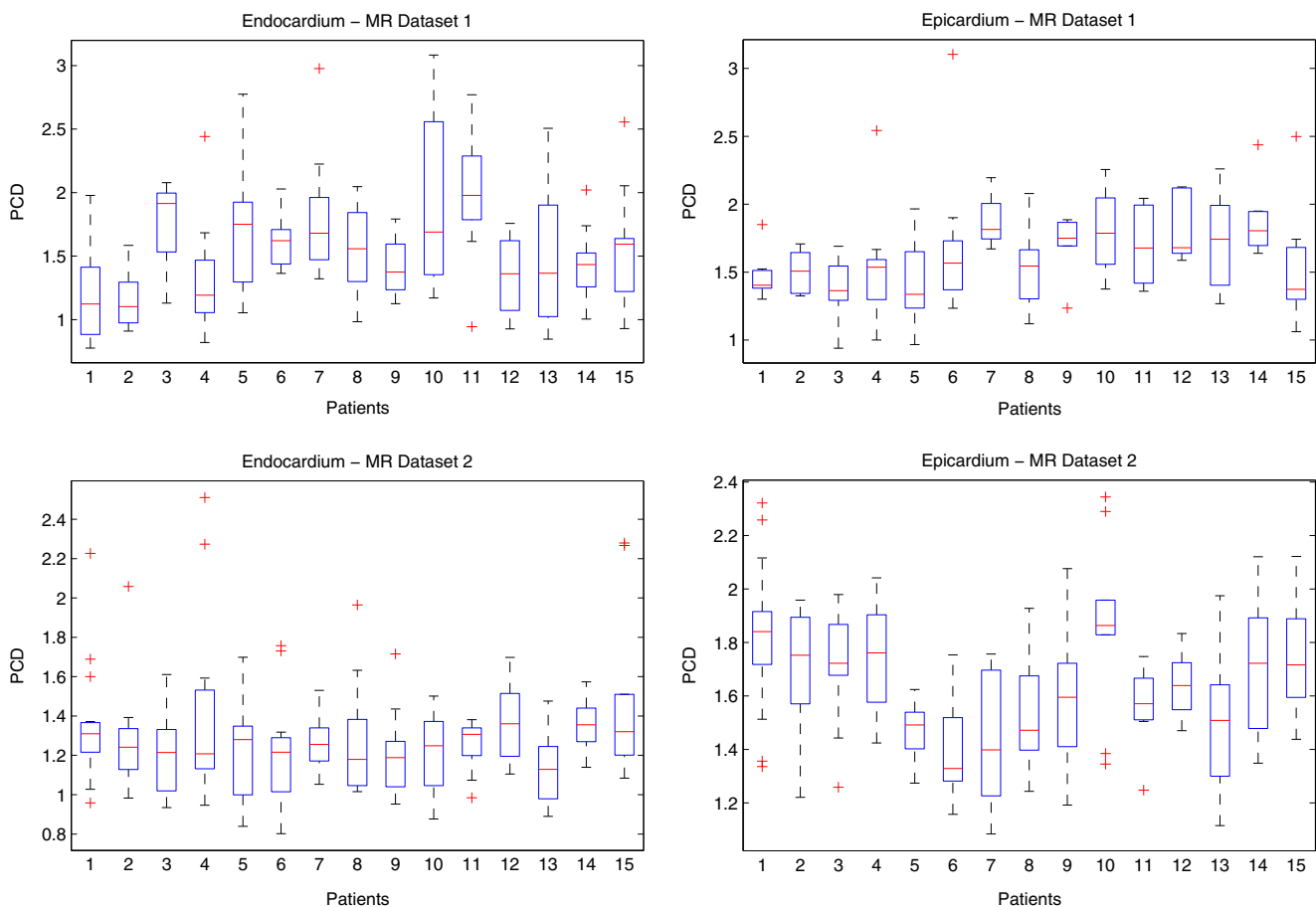
**Fig. 8** Box-Plot graph using the average PCD (mm) metric evaluated with MR data

Table 5 DSC computed for the proposed segmentation approach and two methods of the state of art using MR dataset 2

	Endocardium	Epicardium
Method 1 [36]	0.9000 ± 0.0300	0.9500 ± 0.0100
Method 2 [33]	0.9052 ± 0.0260	0.9261 ± 0.6721
Our method	0.9123 ± 0.0207	0.9291 ± 0.0175

segmentation method for all patients using the PCD metric. It is accepted that a good segmentation is achieved when the computed distance is less than 5 mm [38].

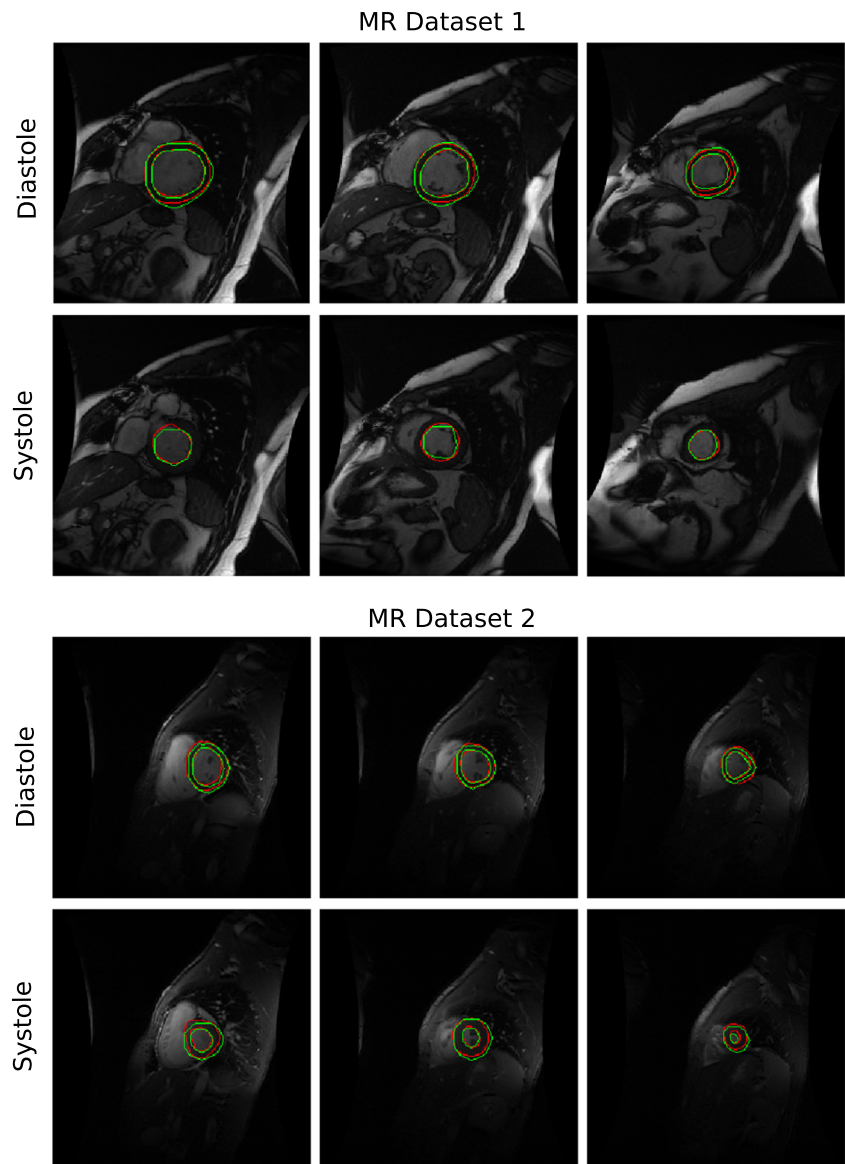
Similarly, results obtained for the second MR dataset are also compared with two different methods of the state of art which used the same database of cardiac MR studies, see Table 5.

Visual performance of the proposed segmentation method is evaluated in Fig. 9. Volume slices selected from each MR dataset are illustrated. The LV is visualized at base, middle and apex of the heart. The red contour is the manual annotation and the green contour is the segmentation obtained with the proposed algorithm.

We also addressed evaluations using a 3D metric. For this purpose, we employed the PSD metric whose results are presented in Table 4 for all MR data. Surface examples obtained from the segmentation are visualized in Fig. 10. Examples are presented for the endocardium at ED and ES phase, and for the epicardium at ED phase.

Bland-Altman analysis was also performed to evaluate the segmentation using clinical indices. The main objective of the segmentation in this application is to provide an efficient mechanism to aid in the cardiac function assessment.

Fig. 9 Visual results for LV segmentation at base (first column), middle (second column) and apex (third column) of the heart for diastole and systole phases using MR volumes



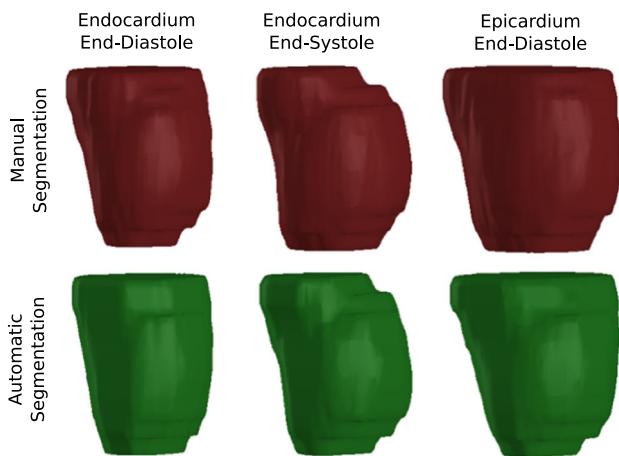


Fig. 10 Surface examples obtained with the segmentation. The red surfaces correspond to the manual segmentation. The green surfaces were obtained using the proposed algorithm

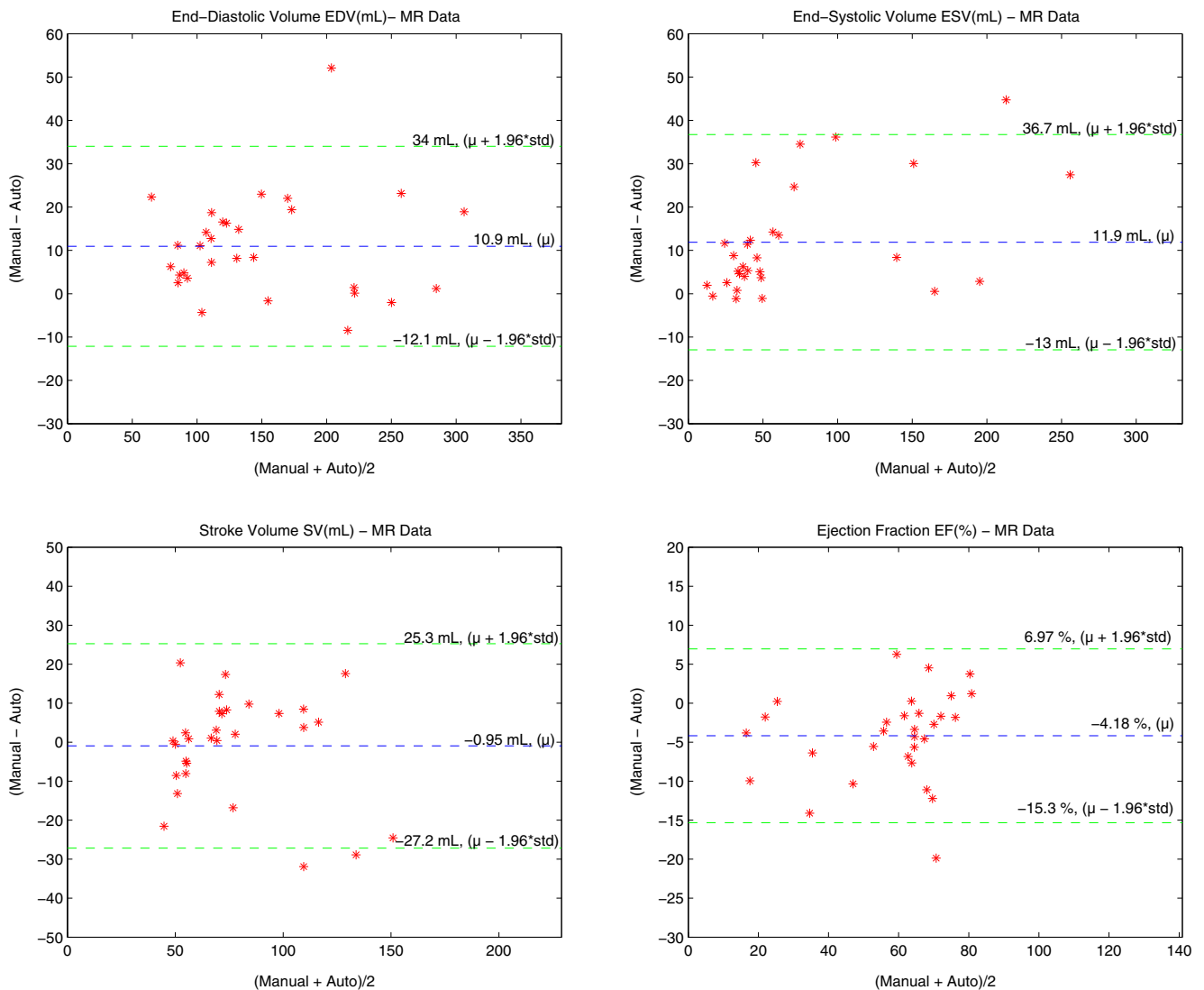


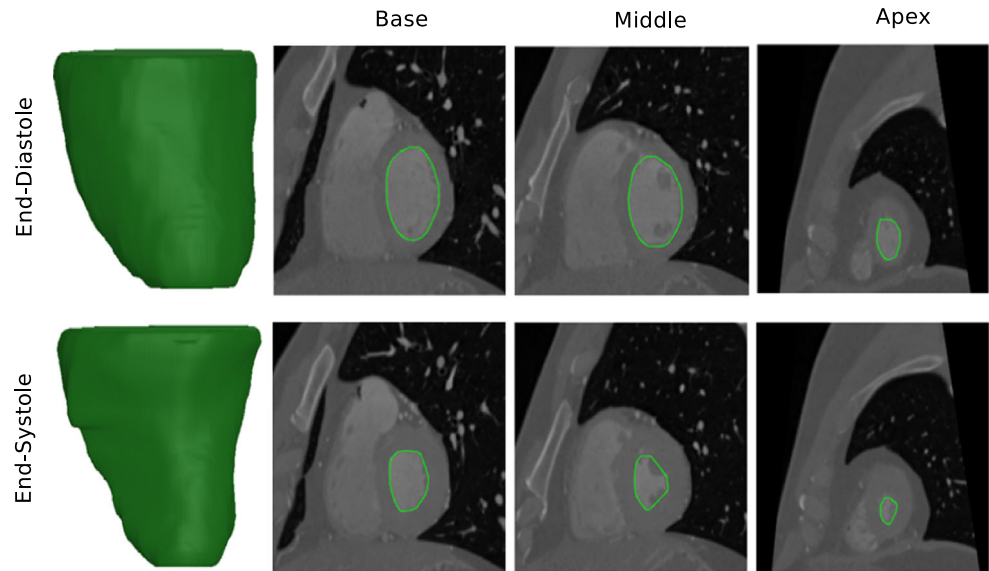
Fig. 11 Bland-Altman graph computed for EDV, ESV, SV, and EF indices using all MR volumes, with μ being the mean and std corresponding to standard deviation. Green lines define the limits of agreement

End-Diastolic Volume (EDV), End-Systolic Volume (ESV), Stroke Volume (SV) and Ejection Fraction (EF) are typical measurements used for LV evaluation [4, 11, 15, 21, 30, 32]. These metrics can be easily computed from the segmentation results. Bland-Altman analysis applied to these clinical indices is depicted in Fig. 11. Here, all volumes gathered from both MR datasets were used.

3.4 CT volumes

We also addressed evaluations of the algorithm using cardiac CT volumes. Results are presented for the LV cavity. Unlike MR studies, the contrast is lower in cardiac CT and boundaries which separate heart structures are more difficult to identify. However, cardiac CT studies present images with bigger size and the number of slices substantially increases, ranging from 80 to 170. Similarly, the

Fig. 12 Segmentation of the LV cavity obtained with the proposed approach using a cardiac CT study. First row: volume and slices at ED phase. Second row: volume and slices at ES phase. Slices are presented for base, middle and apex of the heart



LV cavity is one of the brightest regions in cardiac CT images. On the other hand, cardiac CT images are normally acquired using the original axial view with respect to the human body. This implies that a rotation process is needed in order to provide the short axis view used for LV evaluation. Figure 12 illustrates a segmentation example using the proposed approach. Results for contours are illustrated. The PCD, MHD and PSD obtained are presented in Table 6 for ED and ES phase. Likewise, obtained surfaces are presented in Fig. 12 as well. A Box-Plot graph using the PCD metric is illustrated in Fig. 13 which was also configured to show results for the end-diastolic and end-systolic phases. In addition, Bland-Altman and linear regression analysis using the cardiac clinical indices (EDV, ESV, SV, and EF) are also employed for evaluation whose results are presented in Figs. 14 and 15, respectively.

4 Discussion

The objective of this work is to develop a segmentation algorithm for LV analysis in cardiac MR/CT volumes. The performed experiments demonstrate that the proposed approach is able to extract the LV cavity in CT studies, and the endocardial and epicardial boundaries in MR data. The Box-Plot graph in Fig. 8 and results presented in Table 4 show a PCD less than 2 mm achieved for all evaluated examples using both MR datasets. This value is within the acceptance error which must be less than 5 mm [38] in order to be considered as a good segmentation. The MHD is an alternative distance metric used for performance evaluation. Although this metric presents higher values than PCD, it can be noted that results are still within the acceptance error. The PSD metric was also used for evaluation. Results were

exposed in Table 4 demonstrating the good performance achieved.

In our experiments, we also addressed quantitative comparisons with other methods of the state of art. The DSC metric was used for this purpose. This is one of the most standard metrics used for segmentation evaluation. Most of the authors use this metric for performance assessment. Tables 3 and 5 describe results obtained with the proposed method and others found in the literature. It can be noted that results of our algorithm outperform in most cases the segmentation achieved with the other methods [23, 33, 35, 36, 41]. Unlike the compared methods, we used a generalized scheme which can be configured to be applied satisfactorily to both regions, endocardium and epicardium.

In general, the epicardial boundary is more difficult to detect due to inhomogeneities surrounding the myocardium in these types of cardiac studies. Variability of contrasts and intensities in this region is a direct consequence of different types of tissues connected with the myocardium. Since we are using an AC, we need to prevent leaking problems using a higher weight value for the shape energy (see Table 2).

Figures 9 and 10 illustrate visual results of the segmentation applied to MR data. They are compared with the manual annotation. The obtained contours and surfaces are very close to the manual segmentation.

Table 6 Average PCD and MHD (mm)

	PCD	MHD	PSD
ED Phase	0.9387 ± 0.2507	1.2038 ± 0.7171	0.8035 ± 0.3179
ES Phase	0.9718 ± 0.2133	1.4785 ± 1.0679	0.7848 ± 0.2723

Results for LV cavity at ED and ES phase, using the cardiac CT dataset

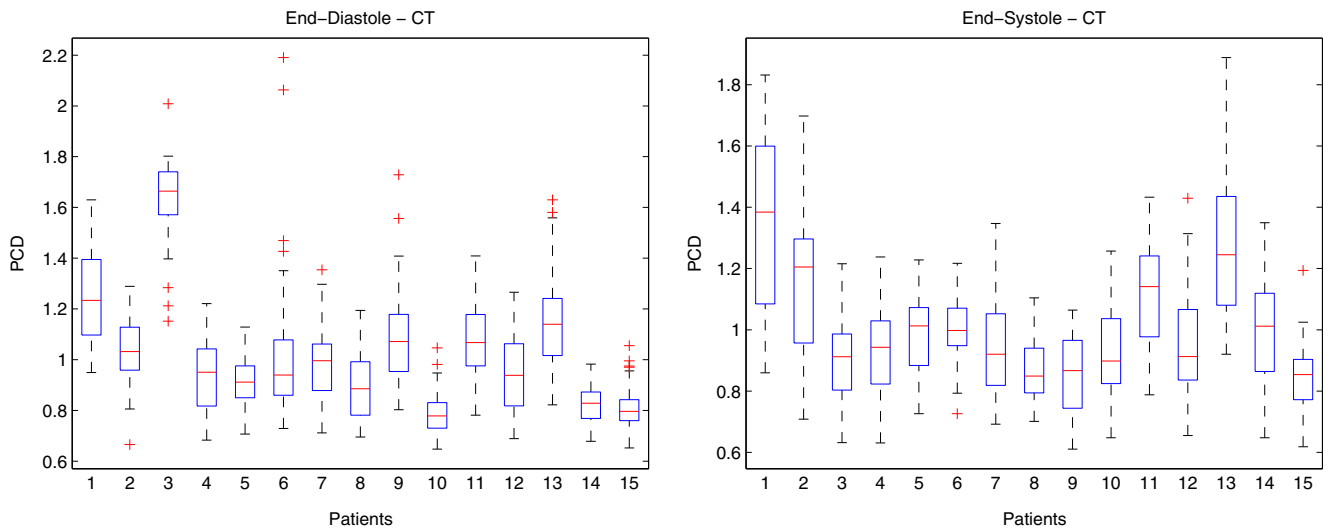


Fig. 13 Box-Plot graph using the average PCD (mm) metric evaluated with CT data

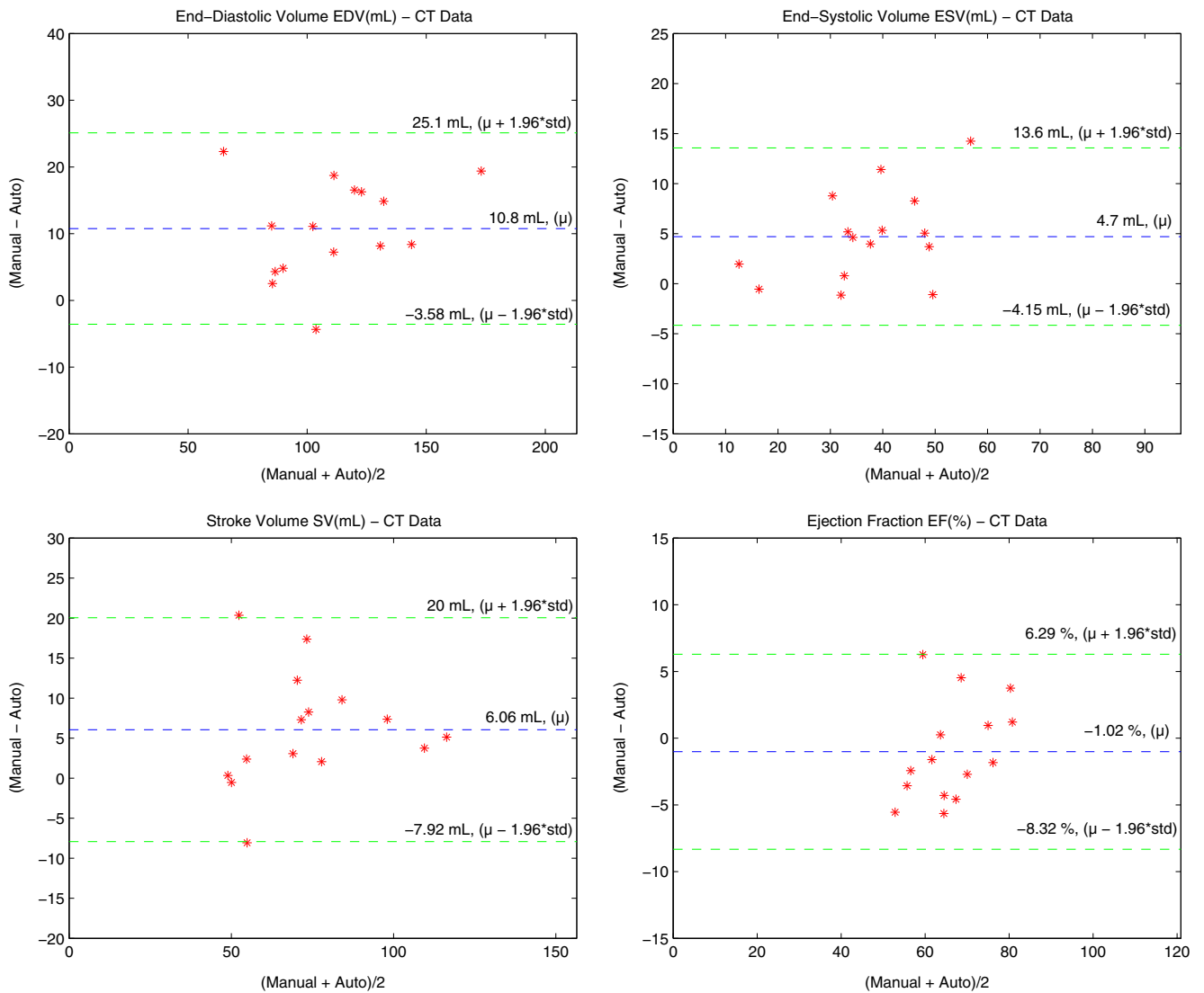


Fig. 14 Bland-Altman graph computed for EDV, ESV, SV, and EF indices using CT volumes

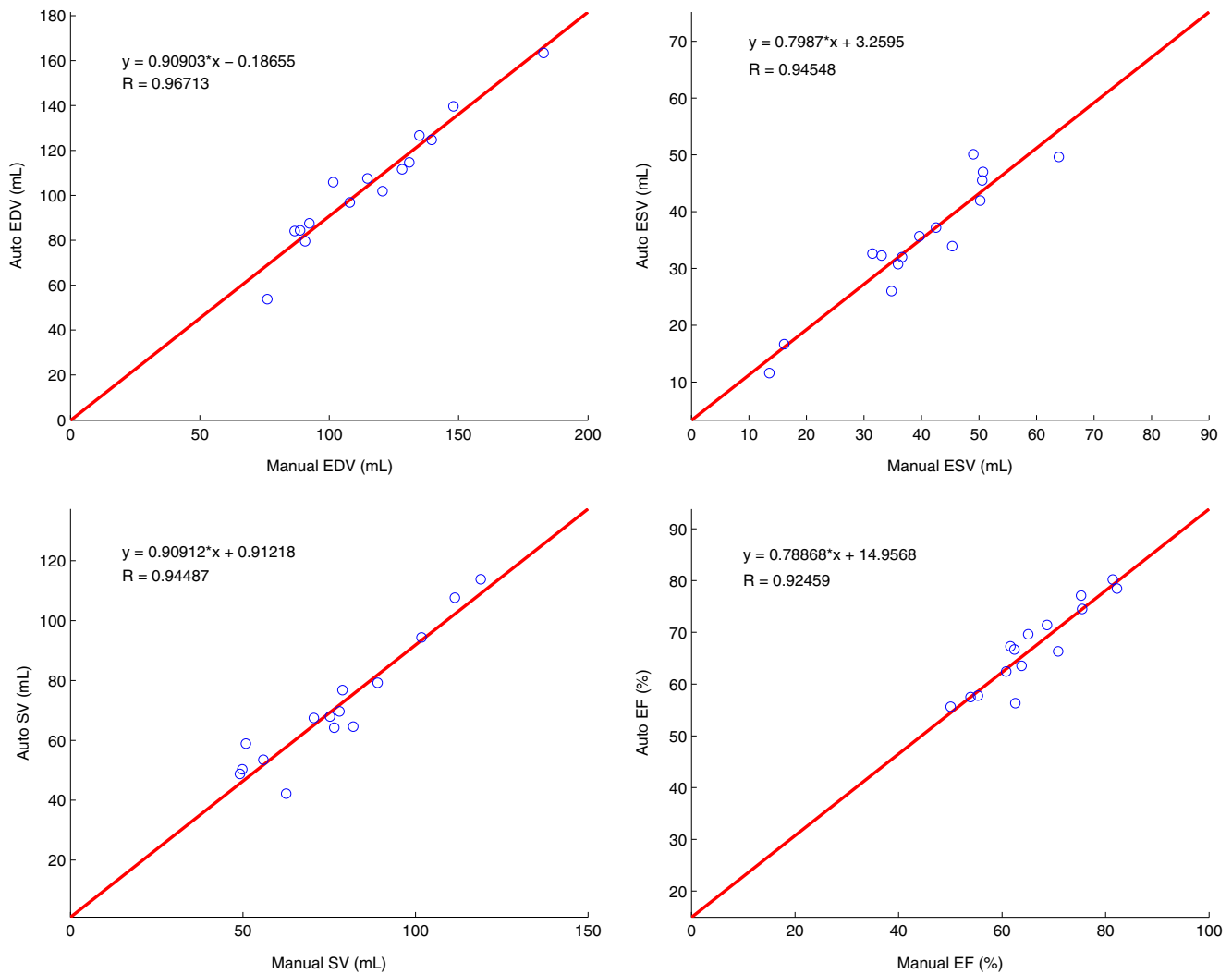


Fig. 15 Linear regression analysis using the manual and automatic segmentation for EDV, ESV, SV and EF

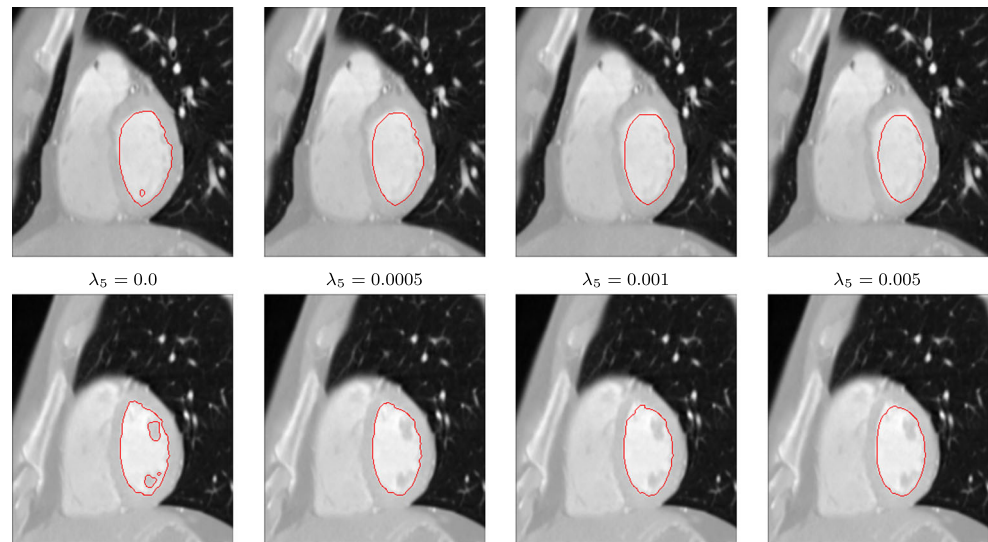
Bland-Altman graph in Fig. 11 shows results using four typical cardiac indices. They have been calculated using all MR volumes. These indices are the final objective of the segmentation since they allow physicians to assess the LV function. It can be seen that most of the evaluated examples lie inside the limits of agreement for all cases.

The algorithm was evaluated using cardiac CT studies as well. Figure 12 shows visual segmentation results for the LV cavity. Figures 14 and 15 illustrate the performance achieved using the clinical indices. Linear regression analysis demonstrates the effectiveness of this work. A high correlation between the manual and automatic segmentation was obtained. Quantitative performance is exposed in Table 6. In general, the LV cavity is more difficult to segment at ES phase. Naturally, the cavity at this stage is more irregular and the size of the papillary muscles appears to be increased with respect to the region covered

by the blood pool. Conversely, the latter characteristic is even problematic for physicians when performing manual segmentations because external boundaries of the papillary muscles are not visible in some parts (see Fig. 12).

Regarding the designed method, the selection process of the algorithm parameters has been made experimentally. It can be noted from Table 2 that more scales were used with the HT when using cardiac CT volumes. In addition, the window size used for the local region energy is bigger. This is logical because the size of volumes in CT is bigger than in MR. Perhaps, the most critical issue regarding the parameter configuration is to assign the weight values for the shape energy. If this value is too high during the first iterations, the AC does not evolve properly because the algorithm tries to maintain the elliptical shape of the interface on each xy -plane. Figure 16 shows the effect of varying the weight value for the shape parameter. Images were taken from a

Fig. 16 Segmentation results using different weight values for the shape parameter. The first row illustrates a basal image. The second row corresponds to an image in the middle of the LV



CT volume. It can be noted that increasing the weight value helps to maintain the elliptical shape of the contour which avoids the segmentation of papillary muscles.

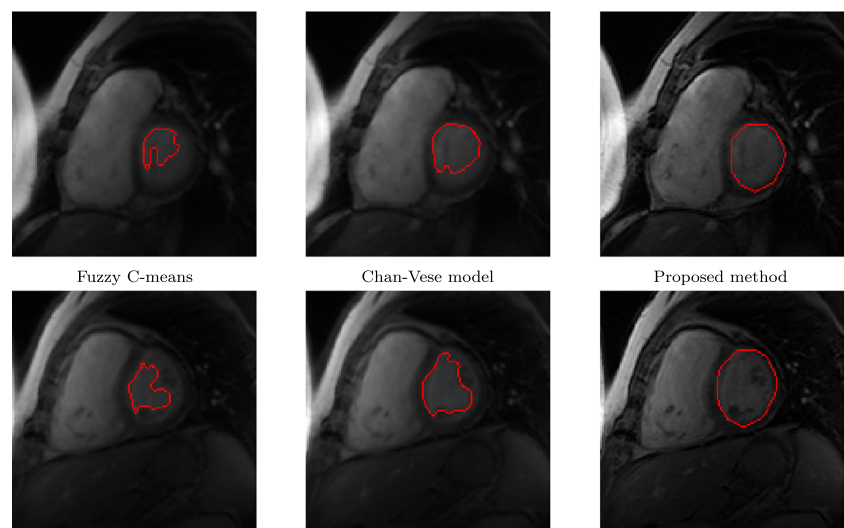
On the other hand, the local region energy can easily handle illumination changes and inhomogeneity problems. It can also be adapted to any type of images. Figure 17 illustrates a comparison between the proposed algorithm and two classical methods (the Chan-Vese model and a Fuzzy C-means algorithm). This comparison was made using a MR volume with inhomogeneity problems. Due to the local region energy, the proposed active contour can handle these issues present in the LV cavity. Even though it is very difficult to provide parameter values without having some knowledge of the input data, it should be very interesting as future work to design an automatic mechanism for this task.

The 3D HT has been used as model for image data coding. The main advantages of this transform are the ability to

provide local direction analysis, multiresolution and multi-scale analysis, different types of texture features, and it is also easy to implement in any dimension. It can be verified in Fig. 2 how the useful information is compressed with the steering process, concentrating most of the energy in a small number of coefficients. In this work, we are employing coefficients until first order but the algorithm can be easily adapted to incorporate more coefficients for this and other applications if needed.

Finally, we are interested in developing an application for evaluating the heart mechanical function using MR and CT studies. As future work, the segmentation will be combined with motion estimation methods with the aim of providing a robust and complete tool which integrates these algorithms and computes different types of clinical indices used for physicians to evaluate the LV function. Some synchronization problems of the LV muscle, and patients with heart

Fig. 17 Results of three methods applied to segmentation of the LV cavity in a MR volume with inhomogeneity problems. Slices at base (first row) and middle (second row) of the heart are presented



failure and cardiac insufficiency can be identified through a clinical quantification of heart structures analyzed with these methods.

5 Conclusion

We have proposed a robust hierarchical multiscale scheme which uses an AC model and the Hermite transform to segment cardiac MR/CT volumes. Experimental results demonstrate the implemented method can be efficiently used for LV evaluation. Several studies taken from two cardiac MR databases and our own CT collection of data were used for validation. As future work, we intend to adapt the algorithm for segmentation of other heart structures and other cardiac views in order to provide a more general framework useful for cardiac evaluation. Given the properties of the HT and the implicit AC, the proposed method can be extended to any dimension.

Funding This work has been sponsored by UNAM grant PAPIIT IN116917 and SECITI grant 110/2015. Leiner Barba-J thanks CONACYT-245976 and Colciencias for financial support.

References

1. AlZubi S, Islam N, Abbod M (2011) Multiresolution analysis using wavelet, ridgelet, and curvelet transforms for medical image segmentation. *Int J Biomed Imaging* 2011(Article ID 136034): 1–18
2. Andreopoulos A, Tsotsos JK (2008) Efficient and generalizable statistical models of shape and appearance for analysis of cardiac MRI. *Med Image Anal* 12(3):335–357
3. van Assen HC, Danilouchkine MG, Frangi AF, Ordás S, Westenberg JJ, Reiber JH, Lelieveldt BP (2006) SPASM: A 3d-ASM for segmentation of sparse and arbitrarily oriented cardiac MRI data. *Med Image Anal* 10(2):286–303
4. Axel L, Kim D (2008) Principles of CT and MRI. In: Marcelo RYK, Di Carli F (eds) *Novel techniques for imaging the heart: Cardiac MR and CT*, chap 1. Wiley-Blackwell, pp 3–16
5. Ayed IB, Li S, Ross I (2009) Embedding overlap priors in variational left ventricle tracking. *IEEE Trans Med Imaging* 28(12):1902–1913
6. Bai W, Shi W, Ledig C, Rueckert D (2015) Multi-atlas segmentation with augmented features for cardiac MR images. *Med Image Anal* 19(1):98–109
7. Bai W, Shi W, O'Regan DP, Tong T, Wang H, Jamil-Copley S, Peters NS, Rueckert D (2013) A probabilistic patch-based label fusion model for multi-atlas segmentation with registration refinement: application to cardiac MR images. *IEEE Trans Med Imaging* 32(7):1302–1315
8. Barba-J L, Moya-Albor E, Escalante-Ramírez B, Brieva J, Venegas EV (2016) Segmentation and optical flow estimation in cardiac CT sequences based on a spatiotemporal PDM with a correction scheme and the Hermite transform. *Comput Biol Med* 69(1):189–202
9. Caselles V, Kimmel R, Sapiro G (1997) Geodesic active contours. *Int J Comput Vis* 22(1):61–79
10. Chan TF, Vese LA (2001) Active contours without edges. *IEEE Trans Image Process* 10(2):266–277
11. Cheung YF (2012) The role of 3D wall motion tracking in heart failure. *Nat Rev Cardiol* 9:644–657
12. Chuang KS, Tzeng HL, Chen S, Wu J, Chen TJ (2006) Fuzzy c-means clustering with spatial information for image segmentation. *Comput Med Imaging Graph* 30(1):9–15
13. Cordero-Grande L, Vegas-Sánchez-Ferrero G, de-la Higuera PC, San-Román-Calvar JA, Revilla-Orodea A, Martín-Fernández M, Alberola-López C (2011) Unsupervised 4D myocardium segmentation with a Markov random field based deformable model. *Med Image Anal* 15(3):283–301
14. Daniel C, Mikael R, Rachid D (2007) A review of statistical approaches to level set segmentation: integrating color, texture, motion and shape. *Int J Comput Vis* 72(2):195–215
15. Dongwoo K, Jonghye W, Slomka PJ, Damini D, Guido G, Kuo C-CJ (2012) Heart chambers and whole heart segmentation techniques: review. *J Electron Imaging* 21(1):010,901–1–010,901–16
16. Dubuisson MP, Jain AK (1994) A modified Hausdorff distance for object matching. In: *Proceedings of the 12th IAPR international conference on pattern recognition, 1994. Conference a: computer vision & image processing, vol 1*, pp 566–568
17. Ecabert O, Peters J, Schramm H, Lorenz C, von Berg J, Walker MJ, Vembar M, Olszewski ME, Subramanyan K, Lavi G, Weese J (2008) Automatic model-based segmentation of the heart in CT images. *IEEE Trans Med Imaging* 27(9):1189–1201
18. Escalante-Ramírez B (2008) The hermite transform as an efficient model for local image analysis: an application to medical image fusion. *Comput Electr Eng* 34(2):99–110. *Advances on Computer-based Biological Signal Processing Techniques*
19. Eslami A, Karamalis A, Katouzian A, Navab N (2013) Segmentation by retrieval with guided random walks: application to left ventricle segmentation in MRI. *Med Image Anal* 17(2):236–253
20. Faghih Roohi S, Aghaeizadeh Zoroofi R (2013) 4D statistical shape modeling of the left ventricle in cardiac MR images. *Int J CARS* 8(3):335–351
21. Gaasch WH, Little WC (2007) Assessment of left ventricular diastolic function and recognition of diastolic heart failure. *Circulation* 116(6):591–593
22. Hu H, Gao Z, Liu L, Liu H, Gao J, Xu S, Li W, Huang L (2014) Automatic segmentation of the left ventricle in cardiac MRI using local binary fitting model and dynamic programming techniques. *PLoS ONE* 9(12):1–17
23. Hu H, Liu H, Gao Z, Huang L (2013) Hybrid segmentation of left ventricle in cardiac MRI using gaussian-mixture model and region restricted dynamic programming. *Magn Reson Imaging* 31(4):575–584
24. Jolly MP (2006) Automatic segmentation of the left ventricle in cardiac MR and CT images. *Int J Comput Vis* 70(2):151–163
25. Lankton S, Tannenbaum A (2008) Localizing region-based active contours. *IEEE Trans Image Process* 17(11):2029–2039
26. Lee HY, Codella NCF, Cham MD, Weinsaft JW, Wang Y (2010) Automatic left ventricle segmentation using iterative thresholding and an active contour model with adaptation on short-axis cardiac MRI. *IEEE Trans Biomed Eng* 57(4):905–913
27. Li C, Kao CY, Gore JC, Ding Z (2008) Minimization of region-scalable fitting energy for image segmentation. *IEEE Trans Image Process* 17(10):1940–1949
28. Martens JB (1990) The hermite transform-theory. *IEEE Trans Acoust Speech Signal Process* 38(9):1595–1606
29. Mitiche A, Ayed IB (2011) *Variational and level set methods in image segmentation*, vol 5. Springer, Berlin
30. Mor-Avi V, Sugeng L, Weinert L, MacEneaney P, Caiani EG, Koch R, Salgo IS, Lang RM (2004) Fast measurement of left ventricular mass with real-time three-dimensional echocardiography: Comparison with magnetic resonance imaging. *Circulation* 110(13):1814–1818

31. Paragios N, Deriche R (2002) Geodesic active regions: a new framework to deal with frame partition problems in computer vision. *J Vis Commun Image Represent* 13(1–2):249–268
32. Petitjean C, Dacher JN (2011) A review of segmentation methods in short axis cardiac MR images. *Med Image Anal* 15(2):169–184
33. Pham VT, Tran TT, Shyu KK, Lin LY, Wang YH, Lo MT (2014) Multiphase B-spline level set and incremental shape priors with applications to segmentation and tracking of left ventricle in cardiac MR images. *Mach Vis Appl* 25(8):1967–1987
34. Pluempitiwiriyaew C, Moura JMF, Wu YJL, Ho C (2005) STACS: new active contour scheme for cardiac mr image segmentation. *IEEE Trans Med Imaging* 24(5):593–603
35. Qian X, Lin Y, Zhao Y, Wang J, Liu J, Zhuang X (2015) Segmentation of myocardium from cardiac MR images using a novel dynamic programming based segmentation method. *Med Phys* 42(3):1424–1435
36. Qin X, Tian Y, Yan P (2015) Feature competition and partial sparse shape modeling for cardiac image sequences segmentation. *Neurocomputing* 149 Part B:904–913
37. Queirós S, Barbosa D, Heyde B, Morais P, Vilaça JL, Friboulet D, Bernard O, D’hooge J (2014) Fast automatic myocardial segmentation in 4D cine CMR datasets. *Med Image Anal* 18(7):1115–1131
38. Radau P, Lu Y, Connelly K, Paul G, Dick A, Wright G (2009) Evaluation framework for algorithms segmenting short axis cardiac MRI. *MIDAS J. Cardiac MR Left Ventricle Segm Chall*. <http://www.midasjournal.org/browse/publication/658>
39. Rosin PL (1993) A note on the least squares fitting of ellipses. *Pattern Recogn Lett* 14(10):799–808
40. Rousson M, Paragios N (2002) Shape priors for level set representations. In: *Computer vision — ECCV 2002: 7th european conference on computer vision copenhagen, denmark, may 28–31, 2002 proceedings, Part II*. Springer, Berlin, pp 78–92
41. Schaerer J, Casta C, Pousin J, Clarysse P (2010) A dynamic elastic model for segmentation and tracking of the heart in MR image sequences. *Med Image Anal* 14(6):738–749
42. Senegas J, Cocosco CA, Netsch T (2004) Model-based segmentation of cardiac MRI cine sequences: a Bayesian formulation. In: *Proceedings of the SPIE*, vol 5370, pp 432–443
43. Silvan-Cardenas JL, Escalante-Ramirez B (2006) The multiscale hermite transform for local orientation analysis. *IEEE Trans Image Process* 15(5):1236–1253
44. Sliman H, Khalifa F, Elnakib A, Soliman A, El-Baz A, Beache GM, Elmaghraby A, Gimelfarb G (2013) Myocardial borders segmentation from cine MR images using bidirectional coupled parametric deformable models. *Med Phys* 40(9):092302
45. Suinesiaputra A, Cowan BR, Al-Agamy AO, Elattar MA, Ayache N, Fahmy AS, Khalifa AM, Medrano-Gracia P, Jolly MP, Kadish AH, Lee DC, Margeta J, Warfield SK, Young AA (2014) A collaborative resource to build consensus for automated left ventricular segmentation of cardiac MR images. *Med Image Anal* 18(1):50–62
46. Suinesiaputra A, Cowan BR, Finn JP, Fonseca CG, Kadish AH, Lee DC, Medrano-Gracia P, Warfield SK, Tao W, Young AA (2012) Left ventricular segmentation challenge from cardiac MRI: a collation study. In: *Statistical atlases and computational models of the heart. Imaging and modelling challenges: Second international workshop, STACOM 2011, held in conjunction with MIC-CAI 2011, Toronto, ON, Canada, September 22, 2011, Revised Selected Papers*. Springer, Berlin, pp 88–97
47. Tavakoli V, Amini AA (2013) A survey of shaped-based registration and segmentation techniques for cardiac images. *Comput Vis Image Underst* 117(9):966–989
48. Tsadok Y, Petrank Y, Sarvari S, Edvardsen T, Adam D (2013) Automatic segmentation of cardiac MRI cines validated for long axis views. *Comput Med Imaging Graph* 37(7–8):500–511
49. Woo J, Slomka PJ, Kuo CCJ, Hong BW (2013) Multiphase segmentation using an implicit dual shape prior: application to detection of left ventricle in cardiac MRI. *Comput Vis Image Underst* 117(9):1084–1094
50. Wu Y, Wang Y, Jia Y (2013) Segmentation of the left ventricle in cardiac cine MRI using a shape-constrained snake model. *Comput Vis Image Underst* 117(9):990–1003
51. Zhu L, Gao Y, Appia V, Yezzi A, Arepalli C, Faber T, Stillman A, Tannenbaum A (2013) Automatic delineation of the myocardial wall from CT images via shape segmentation and variational region growing. *IEEE Trans Biomed Eng* 60(10):2887–2895
52. Zhu L, Gao Y, Appia V, Yezzi A, Arepalli C, Faber T, Stillman A, Tannenbaum A (2014) A complete system for automatic extraction of left ventricular myocardium from CT images using shape segmentation and contour evolution. *IEEE Trans Image Process* 23(3):1340–1351



Leiner Barba-J received his PhD degree in Electrical Engineering from U. Nacional Autónoma de México (2017). His current research interests include computational models for medical image analysis.



Boris Escalante-Ramírez is a Professor at U. Nacional Autónoma de México, PhD from the Technical University of Eindhoven (1992). His research areas include computational models for image processing.



Enrique Vallejo Venegas is a MD from U. Nacional Autónoma de México, Specialist in Internal Medicine and Cardiology. He is mainly interested in evaluating the heart function using cardiac imaging.



Fernando Arámbula Cosío is a Researcher and Lecturer at U. Nacional Autónoma de México, PhD from the Imperial College (1997). He is interested in medical image analysis and computer assisted surgery.